Journal of Structural Biology 183 (2013) 531–536

Contents lists available at SciVerse ScienceDirect

Journal of Structural Biology

journal homepage: www.elsevier.com/locate/yjsbi

Technical Note

Cryomicroscopy of radiation sensitive specimens on unmodified graphene sheets: Reduction of electron-optical effects of charging

Kasim Sader *, Martyn Stopps, Lesley J. Calder, Peter B. Rosenthal *

Division of Physical Biochemistry, MRC National Institute for Medical Research, The Ridgeway, Mill Hill, London NW7 1AA, United Kingdom

ARTICLE INFO

Article history:
Received 12 September 2012
Received in revised form 23 April 2013
Accepted 29 April 2013
Available online 7 May 2013

Keywords:
Graphene
Cryomicroscopy
Charging
Beam induced specimen movement
Radiation damage

ABSTRACT

Images of radiation-sensitive specimens obtained by electron microscopy suffer a reduction in quality beyond that expected from radiation damage alone due to electron beam-induced charging or movement of the specimen. For biological specimens, charging and movement are most severe when they are suspended in an insulating layer of vitreous ice, which is otherwise optimal for preserving hydrated specimens in a near native state. We image biological specimens, including a single particle protein complex and a lipid-enveloped virus in thin, vitreous ice films over suspended sheets of unmodified graphene. We show that in such preparations, the charging of ice, as assessed by electron-optical perturbation of the imaging beam, is eliminated. We also use the same specimen supports to record high resolution images at liquid nitrogen temperature of monolayer paraffin crystals grown over graphene.

1. Introduction: cryomicroscopy requires stable, conductive, transparent supports

Low dose transmission electron cryomicroscopy of unstained, frozen-hydrated specimens in amorphous ice can be applied to high resolution structure determination. However, images recorded of specimens in thin films of ice over micron-sized holes in amorphous carbon suffer a loss of high resolution contrast due to specimen movement or charging (Henderson, 1992). Charging of insulating specimens can degrade images by charge-induced stresses that cause movements of the specimen or electrostatic perturbation of the imaging electron beam. The radiation sensitivity of frozen-hydrated biological specimens requires that images be recorded before charging and beam-induced movement can stabilize.

Improvements in imaging may therefore come from more stable or conductive specimen supports (Miyazawa et al., 1999; Rhinow and Kuhlbrandt, 2008; Yoshioka et al., 2010) or from illumination conditions that reduce charging or movement (Berriman and Rosenthal, 2012; Boettcher, 1995; Miyazawa et al., 1999). Graphene has been proposed as an ideal TEM specimen support because of its electrical conductivity, high strength, and transparency (Geim and Novoselov, 2007). Unmodified graphene has been tested as a support for positively stained (Pantelic et al., 2011b) and air dried (Nair et al., 2010) biomolecules. Altered forms of graphene supports that render them hydrophilic have been tested for imaging unstained frozen-hydrated specimens: graphene oxide (Pantelic et al., 2010), oxidatively-doped graphene (Pantelic et al., 2011a), and nano-crystalline graphene-like membranes (Rhinow et al., 2010, 2011a,b) that contain both graphene and amorphous areas (Turchanin et al., 2011). Images of the test specimen tobacco mosaic virus on oxidatively-doped graphene or nanomembranes are reported to have improvements in high resolution contrast (Pantelic et al., 2011a; Rhinow et al., 2011a). However, unmodified graphene has potential advantages because of its extensively characterized conductivity, strength, thickness, crystallinity, and production.

In this study, we have applied an efficient method of transferring monolayer CVD graphene to holey carbon films for use as a support for minimum dose imaging of radiation sensitive specimens, including biological specimens vitrified in thin films over unmodified graphene. We show that with a graphene support present the charging of the ice film, as assessed by beam expansion of the defocused diffraction pattern (Berriman and Rosenthal, 2012; Brink et al., 1998), is eliminated. We also show that high resolution images of the radiation-sensitive organic crystal paraffin can be obtained by cryomicroscopy of crystals grown on graphene.

2. Preparation of frozen-hydrated biological specimens in amorphous ice over unmodified graphene sheets

CVD monolayer graphene on Cu foil (Graphene Supermarket; CVD-Cu-2x2) was transferred to gold Quantifoil electron

* Corresponding authors. Present address: FEI, Eindhoven, The Netherlands (K. Sader).

E-mail addresses: kasim.sader@gmail.com (K. Sader), prosent@nimr.mrc.ac.uk (P.B. Rosenthal).

1047-8477
http://dx.doi.org/10.1016/j.jsb.2013.04.014

microscopy grids using methods similar to those previously described (Pantelic et al., 2011b), except that we designed and fabricated a single cell flow chamber for transfer of the graphene to multiple grids with reduced handling. The grids were annealed to the graphene by adding drops of chloroform to grids placed with the carbon side of the grid toward the graphene and heating to 200–250 °C in air for 10–20 min (Regan et al., 2010). The annealed grids on graphene were coated with a film of 0.5% w/w Formvar/chloroform to add stability during Cu removal as previously described (Pantelic et al., 2011b; Regan et al., 2010). Fig. 1(a–c) shows dissolution of the Cu foil by the flow of $FeCl_3$ (Farnell AR413 37–46%), revealing grids with the graphene side up and attached to a Formvar film (Pantelic et al., 2011b). Dissolution of Cu was followed by extensive but gentle washing with analytical grade water (Fig. 1d–f) and without movement of the graphene/Quantifoil/Formvar layer. Fig. 1f shows grids attached to the Formvar sheet that may be dissolved by chloroform before additional wash steps with ethyl acetate, chloroform, or concentrated HCl are applied to individual grids. The resulting specimen support has an amorphous carbon side adjacent to the grid bars and a graphene layer on the side of the carbon that is distal to the grid bars (Fig. S1, Supporting Information).

When examined in the electron microscope, the contrast of clean graphene sheets is very low, and displaced objective aperture, dark field TEM was used to identify grids with holes covered with clean graphene (Fig. 1g). The procedure achieves large areas of homogenous coverage of the grid with graphene. Electron diffraction of holes with suspended graphene sheets shows the signature hexagonal pattern of graphene. The ratios of the 2.13 Å and 1.23 Å reflections as well as the diffraction pattern of tilted specimens are indicative of a monolayer (Meyer et al., 2007) (Fig. S2, Supporting Information). The appearance of the graphene and diffraction patterns are unchanged following electron irradiation at 120 keV and 200 keV (at least 2.4×10^3 $e^-/Å^2$ at 120 keV), many times the exposure used in low dose imaging.

We used these graphene grids without further modification or glow discharging as a support for vitrification and low dose imaging and tomography of several biological specimens. 3–5 μl samples of influenza virus (C/JHB/1/66) or 5 mg/ml solution of apoferritin (Sigma A-3641) were applied through the grid bars to the amorphous carbon side of the grid, which is more hydrophilic than the continuous graphene side, and plunge frozen (Vitrobot Mark III, FEI, 4 °C, 95% relative humidity, 2–4 s blot time). Alternatively, apoferritin was added to the continuous graphene side and plunge frozen after lightly evaporating amorphous carbon (2×100 ms current pulses applied to carbon rods in an Emitech K950X) to make the graphene side more hydrophilic.

Electron cryomicroscopy was performed at liquid nitrogen temperature either on an FEI Tecnai Spirit microscope operating at 120 keV with a tungsten source, Eagle 2K CCD, and a Gatan 626 cryoholder or on an FEI G2 Polara field emission gun microscope operating at 200 keV with a Tietz F224HD CCD camera. Tilt series of influenza virus (7 μm defocus, 6.0 Å/pixel) or apoferritin (6 μm defocus, 4.4 Å/pixel) with accumulated dose of 50–100 $e^-/Å^2$ were acquired on the Polara using SerialEM (Mastronarde, 2005) and processed using IMOD (Mastronarde, 1997). Diffraction measurements were performed at a long camera length (~2.5 m).

A low magnification image shows a grid square of frozen hydrated influenza virus (Fig. 2a) with holes covered by amorphous ice. Sections from a tomogram parallel to the plane of the amorphous ice show 100 nm sized virions with a membrane and a glycoprotein layer (Fig. 2b). The ice thickness was measured to be 120 nm from sections of the tomogram perpendicular to the plane of the ice (Fig. 2c). Similar measurements on two additional tomograms of 130 and 170 nm were consistent with the virions being fully embedded in the ice. The diffraction pattern in Fig. 2d shows both hexagonal reflections from graphene and diffuse diffraction rings of amorphous ice but devoid of crystalline ice peaks. The ring spacings of amorphous ice on graphene were calibrated using the internal standard of the graphene spacings (2.13 Å) and measured using the Digital Micrograph™ plug-in DiffTools (Mitchell, 2008) to be 3.7 ± 0.1 Å and 2.14 ± 0.06 Å (9 measurements), consistent with low density amorphous ice (Dubochet et al., 1988). Fig. 3a and b show images of apoferritin, a 450 kDa 24-mer protein assembly that forms a hollow shell, visible as ~100 Å diameter spheres. In Fig. 3a the hole is partially covered by graphene with amorphous ice over graphene (top) and unsupported amorphous ice film (bottom); the graphene is folded at the boundary. Fig. 3c shows a diffraction pattern of the specimen in 3b with hexagonal graphene reflections and amorphous ice rings with spacings 3.68 ± 0.04 Å and 2.14 ± 0.02 Å (9 measurements) similar to those for the influenza sample. Fig. 3d shows a section of a tomogram parallel to the plane of the ice film with apoferritin particles visible. Fig. 3e shows a section perpendicular to the plane of the film where the apoferritin particles are slightly elongated due to the missing data wedge, but present in ice approximately 250 Å thick.

The specimens are embedded in an amorphous ice layer and are typical of those prepared in our laboratory using standard holey films. For images such as Fig. 3b, no objective aperture was used and images were taken in each hole without the beam touching

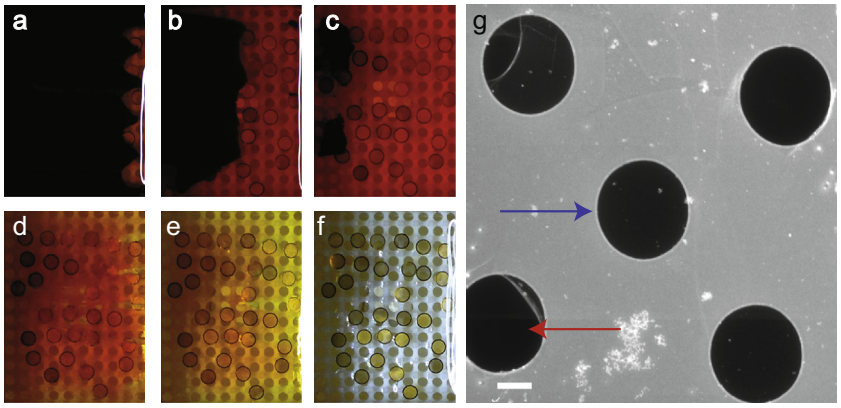

Fig.1. Transfer of monolayer CVD graphene to gold Quantifoil grids in a flow cell. (a) Cu foil covered in $FeCl_3$ with visible etching on the right side. (b) Further progression of etching showing half of the Cu foil removed. (c) Most of the Cu foil has been dissolved. (d) Initial washing step after mixing of the $FeCl_3$ and water. (e) $FeCl_3$ partially removed. (f) Clean grids (diameter 3.05 mm) with graphene side up remain attached to the formvar sheet in water. (g) Displaced aperture dark field TEM image showing graphene suspended over holes (blue arrow) and a hole without graphene (red arrow). (Scale bar 1 μm).

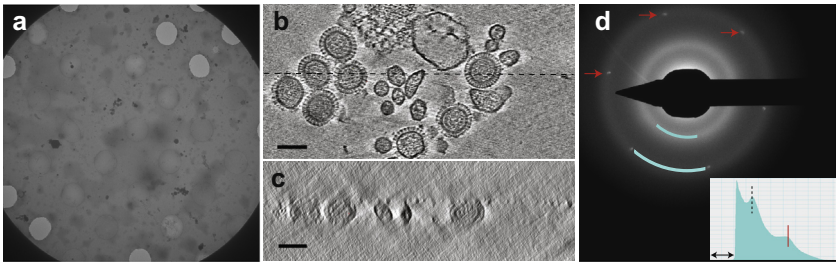

Fig.2. Frozen-hydrated influenza virus over graphene. (a) Low magnification image of a grid square with 3 μm diameter holes covered by amorphous ice and empty holes. (b) Sections of a tomogram (24 nm thick) parallel to the plane of the amorphous ice with influenza virions. (c) Sections of a tomogram (13 nm thick) perpendicular to the plane of the ice along the dotted line in b. (d) Diffraction pattern shows hexagonal graphene reflections at 2.13 Å (red arrows) and diffuse amorphous ice rings (blue arcs at 3.7 Å and 2.14 Å resolution). (inset) Radial average of the pattern within a sector that excludes graphene reflections (as indicated by arcs along amorphous ice maxima) with first ice maximum (dotted vertical line) and the resolution of graphene reflections (2.13 Å, vertical red line) indicated. Horizontal arrow shows region obscured by beamstop. Scale bars 100 nm.

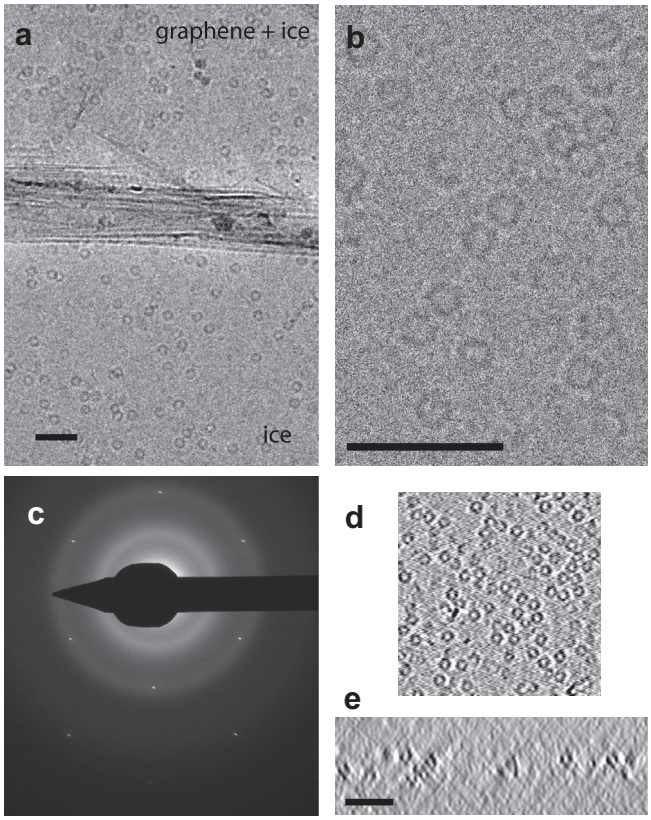

Fig.3. Frozen-hydrated apoferritin over graphene. (a) Low dose image of apoferritin applied to the amorphous carbon side of the grid. The graphene layer spans only part of the ice film (top) and is folded at the boundary. (b) Image of apoferritin applied to the graphene film after light carbon evaporation, 3 μm defocus and 10 $e^{-}/Å^2$. (c) Diffraction pattern showing hexagonal graphene reflections and diffuse amorphous ice rings. (d) Section of tomogram parallel to the plane of the amorphous ice showing apoferritin particles. (e) Section of tomogram perpendicular to the plane of the ice. Apoferritin particles are elongated due to the missing data wedge, but present at different depths within the ice film. Scale bars 50 nm.

the adjacent thick Quantifoil carbon support, conditions known to exhibit charging on ice films (Berriman and Rosenthal, 2012; Boettcher, 1995). As the images from these grids with suspended graphene sheets did not show visible effects of charging such as blurring, we next sought to study directly the extent of charging.

3. Elimination of the electron-optical effects of charging for amorphous ice specimens

Charging was measured by its electron-optical effects in defocused diffraction mode as previously described (Berriman and Rosenthal, 2012; Brink et al., 1998). Beam-induced ejection of secondary electrons causes a saturable positive charge build-up on thin insulators in TEM (Cazaux, 1995), which deflects the beam. Positive charge on the specimen acts as an electrostatic lens causing an effective change in the focal length of the objective lens. In diffraction mode, the focal length change results in a change in the diameter of the low resolution image formed by defocusing the zero order diffraction spot. A change in diameter of the defocused diffraction image is therefore a sensitive measure of charge. When the beam irradiates the thick amorphous carbon adjacent to a hole, the defocused diffraction image is the same size as when the beam irradiates no support (vacuum) indicating no charge build-up. We compared the difference in charge build-up on holes covered by amorphous ice or amorphous ice with graphene when charging had reached equilibrium.

We recorded series of defocused diffraction images in which the beam successively irradiated the carbon support, the amorphous ice, and then the carbon support for holes uniformly distributed on the 3 different grids (>20 measurements) shown in Figs. 2 and 3. When imaging a hole covered by amorphous ice by a beam irradiating ice only without touching the adjacent carbon support, charging causes a 3–15% reversible increase in the defocused diffraction image compared to one recorded over the adjacent carbon support. Fig. 4a shows a 10% increase in beam diameter due to charging. The diffraction pattern in Fig. 4b shows that the hole contains amorphous ice only and no graphene. When imaging a hole covered by amorphous ice on the same grid and with the same illumination but with a graphene support, no beam expansion was observed (Fig. 4c, <1% change in diameter of defocused diffraction spot, diffraction pattern in Fig. 4d). This difference was not due to a variation in ice thickness, because the difference in percent transmission between the holes was less than 1%.

By contrast, a commercially available 2 nm amorphous carbon film supplied by Quantifoil on S7/2 grids severely charges as judged by beam expansion, with or without an amorphous ice layer, and whether at room or liquid nitrogen temperature (Fig. S3, Supporting Information).

The addition of a graphene support thus eliminates the electron optical effect due to uncompensated charging of amorphous ice that causes a change of size in the defocused diffraction image. Though the amount of beam expansion due to charging is dependent on the choice of diffraction lens underfocus and camera length, the compensation of charging correlated perfectly with the presence of intact graphene under every condition tested. Subsequently, we were able to use the elimination of beam changes as an indication of an underlying graphene substrate as it can be difficult to distinguish amorphous ice supported by graphene and unsupported amorphous ice in a low dose, low magnification image due to graphene's transparency (>50 measurements on grids shown in Figs. 2 and 3).

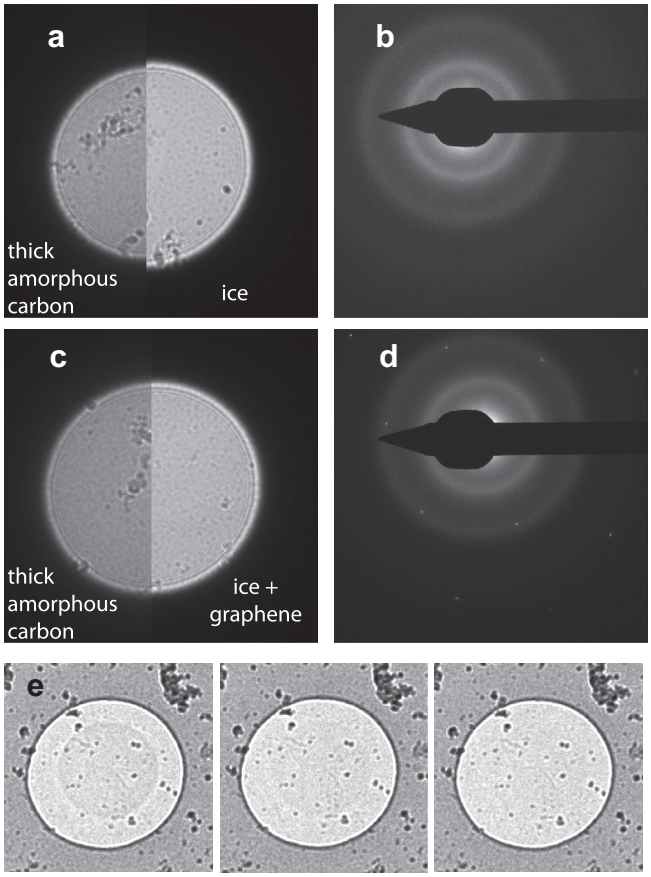

Fig.4. Comparison of charging of amorphous ice with amorphous ice over a graphene sheet by electron optical perturbation of image in defocused diffraction mode. (a) Composite showing 10% change in diameter between defocused diffraction image of amorphous carbon (half profile, left) and amorphous ice (half profile right). (b) Diffraction pattern showing amorphous ice rings for same hole as (a). (c) A composite showing no change in diameter between defocused diffraction image of amorphous carbon (half profile, left) and amorphous ice over graphene (half profile, right). (d) Diffraction pattern showing amorphous ice rings and graphene reflections for same hole as (c). (e) Phase contrast effect due to charging following irradiation of circular area on graphene at −196 °C with 5 $e^-/Å^2$. Defocused diffraction images showing strong contrast (panel 1) on first exposure with footprint fading on second (panel 2) and third (panel 3) exposures that irradiate a much larger region than the hole.

One possible mechanism of charge compensation by graphene is the accumulation of negative charge in the graphene layer adjacent to the positive charge on the ice, forming a dipole layer, as has been described for insulators covered by a thin conducting layer (Cazaux, 1995; Glaeser and Downing, 2004). Secondary electrons from irradiation of the adjacent amorphous carbon have also been demonstrated to compensate for electron optical effects in ice (Berriman and Rosenthal, 2012). Because graphene compensates charging even without irradiation of the adjacent carbon, a compensating mechanism by secondary electrons would require that they are emitted from the graphene layer, despite its low secondary electron emission yields (Luo et al., 2011). Mobility of charges within the ice layer or beam-induced conductivity of ice may also play a role.

4. Cryomicroscopy of a two-dimensional organic crystal on graphene

The radiation sensitive organic crystal paraffin, which is a monolayer 58 Å thick, has been used as a test specimen for imaging radiation sensitive specimens (Dorset and Zemlin, 1985; Glaeser et al., 2011; Henderson and Glaeser, 1985). Monolayer paraffin crystals were prepared by adding a 5 μl drop of hexane saturated with paraffin ($C_{44}H_{90}$ – tetratetracontane, Supelco, LB67780) to a Quantifoil-graphene grid, in some cases wicked with filter paper and others left to dry as previously described (Glaeser et al., 2011). The paraffin crystals cover the graphene over holes as well as the adjacent carbon support. We have obtained images and diffraction patterns of crystalline paraffin supported by graphene under typical microscope conditions used for vitreous specimens at −196 °C on the Polara microscope operating at 200 keV. Fourier transforms of images show that the paraffin lattice dimensions (a = 7.4 Å, b = 5.0 Å), calibrated using the 2.13 Å graphene reflections, are similar to those described previously (Dorset and Zemlin, 1985; Glaeser et al., 2011).

For the diamond-shaped crystal shown in Fig. 5a, a defocused diffraction pattern (1 $e^-/Å^2$) shows several orders of reflections from the paraffin lattice (Fig. 5b), with crystalline imperfections evident as dark areas within the defocused reflections. All ~4 Å reflections are present in the power spectrum of an image recorded of a smaller area of the crystal (178 × 178 nm) with an exposure of 3 $e^-/Å^2$ (Fig. 5c). In some exposures, higher resolution reflections are observed (Fig. 5d). Fig. 5e shows a focused electron diffraction pattern of the same area from which the image was recorded showing ~4 Å paraffin reflections (red arrows) and graphene reflections (white arrows). After further accumulated dose (Fig. 5f), the ~4 Å paraffin reflections have mostly faded and the graphene reflections have remained constant.

We routinely found all ~4 Å reflections (3.7 Å, 4.1 Å) in the Fourier transforms of images, a feature of good paraffin images according to previous studies of paraffin on amorphous carbon (Glaeser et al., 2011), and intensity measurements of several of the best images are shown in Table S1. Quantitative measurements attribute the loss of high resolution (~4 Å) image contrast to beam-induced movements based on comparison to electron diffraction patterns for which the integrated intensities are not affected by such movements (Glaeser et al., 2011; Henderson and Glaeser, 1985). From image transforms, we evaluated the ratio of the ~4 Å structure factor amplitude to the origin peak, F(g)/F(0), a measure of image quality, and estimate that the highest value observed exhibits 25% of the contrast anticipated for images not degraded by movements during exposure (See Supporting Methods). The data are promising in showing that high resolution imaging of beam sensitive specimens can be achieved on graphene. In a recent study of paraffin crystals (Glaeser et al., 2011), the use of a thick amorphous carbon film support (35 nm) was shown to eliminate beam induced contrast loss presumably due to either increased conductivity or stability of the support. Though not yet showing the perfect contrast reported for 35 nm carbon supports (Glaeser et al., 2011), holey carbon films with suspended graphene sheets merit further study for optimizing the imaging of radiation sensitive crystals. In addition to conductivity and stability, graphene monolayers have reduced inelastic scattering compared to amorphous carbon supports and elastic scattering confined to graphene lattice reflections at high resolution.

The paraffin grids were not covered with thick ice that charges and causes electrostatic effects as described in the last section. In highly defocused diffraction mode, however, we observed beam "footprints" (Fig. 4e), similar to those previously observed over amorphous carbon supports, where it has been demonstrated to be a phase contrast effect due to charge and not irradiation-induced contamination or etching (Brink et al., 1998; Downing et al., 2004). The footprint (Fig. 4(e), panel 1) is formed by concentrated irradiation by a beam that touches only the graphene film. The footprint remains without discharging, and fades only upon subsequent exposures when a wide region including the amorphous carbon support is irradiated (Fig. 4e, panels 2 and 3). The

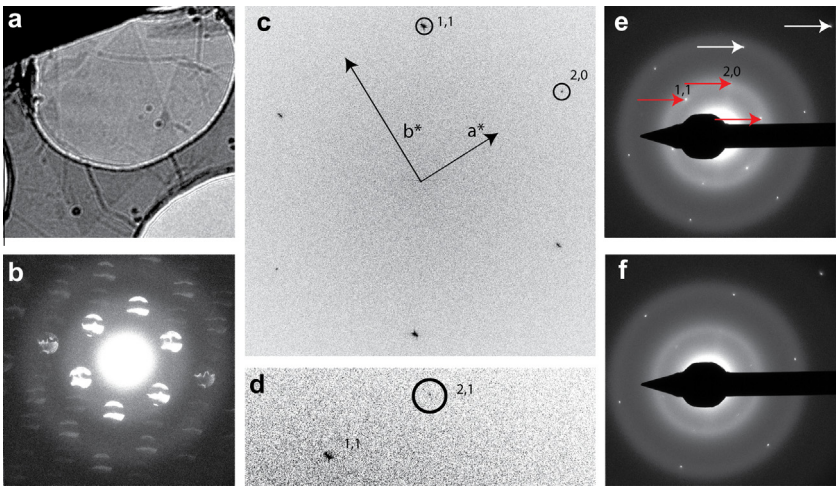

Fig.5. Imaging paraffin crystals grown on graphene-covered holey carbon grids. (a) Low magnification image of a diamond-shaped monolayer paraffin crystal grown over a 3 μm Quantifoil hole covered by graphene. (b) 1 $e^-/Å^2$ defocused diffraction pattern of part of the diamond crystal in (a) showing several orders of reflections from the paraffin lattice. (c) Power spectrum from image of a 178 × 178 nm crystal area much smaller than for the diffraction pattern taken with 3 $e^-/Å^2$ showing the (1,1) at 4.1 Å, (1,−1) at 4.1 Å, and (2,0) at 3.7 Å. Reciprocal lattice vectors are indicated with arrows. (d) Small area of power spectrum of image (20120503_19), recorded prior to image for (c) with exposure of 1 $e^-/Å^2$, displays a 3.0 Å (2,1) reflection. (e) 10 $e^-/Å^2$ focused electron diffraction pattern with labels on upper half showing graphene reflections (white arrows) and paraffin reflections (red arrows). (f) 10 $e^-/Å^2$ focused electron diffraction pattern after an accumulated dose of 45 $e^-/Å^2$ showing the paraffin reflections mostly faded, but the graphene reflections unchanged.

net amount of residual charge in footprints is negligible compared to the uncompensated charge over ice, as there is no effect on the size of the defocused diffraction image over graphene or the thick amorphous carbon. The observation of beam "footprints" on graphene sheets suggests that insulating material on the graphene surface charges and, despite compensation by the graphene layer, causes a phase contrast effect of the type that is also found on amorphous carbon films (Brink et al., 1998; Downing et al., 2004). Further investigation of this effect may require pristine graphene.

5. Application and prospects

The transfer of CVD monolayer graphene to Quantifoil grids (Pantelic et al., 2011b) yields a specimen support suitable for plunge freezing and imaging frozen-hydrated biological specimens by low dose methods. When used in diffraction studies of crystals or amorphous materials, the graphene reflections also provide an internal camera length calibration. Evaluation of the best sample preparation method and conductive films, including the relative merits of unmodified graphene compared to modifications that make the graphene hydrophilic requires further investigation. Unmodified graphene has potential advantages because of its extensive characterization and production. In preparing thin films of amorphous ice over holey carbon films, the spreading of the buffer and the suspension of molecules over empty holes prior to blotting and freezing is influenced by the properties of the surface and the extent of blotting. When the specimen is applied to the amorphous carbon side of the Quantifoil-graphene grids, the properties of the amorphous carbon may be used to control the formation of amorphous ice films over graphene sheets as reported for nanomembranes (Rhinow et al., 2011b). As shown here in tomogram cross-sections for frozen-hydrated specimens of different thicknesses, the sample is suspended in the thin ice film and need not adhere directly to the specimen support.

We show that an electron optical beam-induced imaging artefact caused by charging of amorphous ice is compensated by an underlying graphene support. Graphene sheets form a complete and continuous covering of individual holes, providing a conductivity path for electrons from grid bars and the adjacent amorphous carbon support. Multiple high magnification images can be acquired from the same hole without illumination of the adjacent thick amorphous carbon support. Graphene supports may thus facilitate other approaches to reduce beam-induced movement, such as serial scanning of small areas of the specimen (spotscan – imaging) (Bullough and Henderson, 1987; Downing and Glaeser, 1986), which is reported to reduce movements in 2D crystalline specimens, but is not ordinarily used for non-crystalline specimens in amorphous ice because of problematic charging (Zhou et al., 1994). The lack of temperature dependence of these properties (Geim and Novoselov, 2007) suggests that graphene may also compensate charging in cryomicroscopy experiments at liquid helium temperature, where charging is worse because amorphous carbon supports are poorly conducting (Rader and Lamvik, 1992). The well-defined properties of graphene are important in understanding the mechanism of charging and charge compensation during the electron irradiation of insulators such as amorphous ice and in understanding the relationship between charging and other sources of beam-induced motion (Brilot et al., 2012). We expect further experiments on graphene supports to extend the limits of electron cryomicroscopy of beam sensitive biological specimens.

Acknowledgments

This work was funded by the Medical Research Council (UK) under program code U117581334. We thank A. Lang, J. Berriman, R. Henderson, T. Grant, V. Nicolosi, J. Rubinstein, J. Molloy, and for discussions. We are grateful for access to facilities at LEMAS (Leeds) and SuperSTEM.

Appendix A. Supplementary data

Supplementary data associated with this article can be found, in the online version, at http://dx.doi.org/10.1016/j.jsb.2013.04.014.

References

Berriman, J.A., Rosenthal, P.B., 2012. Paraxial charge compensator for electron cryomicroscopy. Ultramicroscopy 116, 106–114.
Boettcher, B., 1995. Electron cryo-microscopy of graphite in amorphous ice. Ultramicroscopy 58, 417–424.

Brilot, A.F., Chen, J.Z., Cheng, A., Pan, J., Harrison, S.C., Potter, C.S., Carragher, B., Henderson, R., Grigorieff, N., 2012. Beam-induced motion of vitrified specimen on holey carbon film. J. Struct. Biol. 177, 630–637.

Brink, J., Sherman, M.B., Berriman, J., Chiu, W., 1998. Evaluation of charging on macromolecules in electron cryomicroscopy. Ultramicroscopy 72, 41–52.

Bullough, P., Henderson, R., 1987. Use of spot-scan procedure for recording low-dose micrographs of beam-sensitive specimens. Ultramicroscopy 21, 223–230.

Cazaux, J., 1995. Correlations between ionization radiation damage and charging effects in transmission electron microscopy. Ultramicroscopy 60, 411–425.

Dorset, D.L., Zemlin, F., 1985. Structural changes in electron-irradiated paraffin crystals at <15 K and their relevance to lattice imaging experiments. Ultramicroscopy 17, 229–235.

Downing, K.H., Glaeser, R.M., 1986. Improvement in high resolution image quality of radiation-sensitive specimens achieved with reduced spot size of the electron beam. Ultramicroscopy 20, 269–278.

Downing, K.H., McCartney, M.R., Glaeser, R.M., 2004. Experimental characterization and mitigation of specimen charging on thin films with one conducting layer. Microsc. Microanal. 10, 783–789.

Dubochet, J., Adrian, M., Chang, J.J., Homo, J.C., Lepault, J., McDowall, A.W., Schultz, P., 1988. Cryo-electron microscopy of vitrified specimens. Q. Rev. Biophys. 21, 129–228.

Geim, A.K., Novoselov, K.S., 2007. The rise of graphene. Nat. Mater. 6, 183–191.

Glaeser, R.M., Downing, K.H., 2004. Specimen charging on thin films with one conducting layer: discussion of physical principles. Microsc. Microanal. 10, 790–796.

Glaeser, R.M., McMullan, G., Faruqi, A.R., Henderson, R., 2011. Images of paraffin monolayer crystals with perfect contrast: minimization of beam-induced specimen motion. Ultramicroscopy 111, 90–100.

Henderson, R., 1992. Image contrast in high-resolution electron microscopy of biological macromolecules: TMV in ice. Ultramicroscopy 46, 1–18.

Henderson, R., Glaeser, R.M., 1985. Quantitative-analysis of image-contrast in electron-micrographs of beam-sensitive crystals. Ultramicroscopy 16, 139–150.

Luo, J., Tian, P., Pan, C.-T., Robertson, A.W., Warner, J.H., Hill, E.W., Briggs, G.A.D., 2011. Ultralow secondary electron emission of graphene. ACS Nano 5, 1047–1055.

Mastronarde, D.N., 1997. Dual-axis tomography: an approach with alignment methods that preserve resolution. J. Struct. Biol. 120, 343–352.

Mastronarde, D.N., 2005. Automated electron microscope tomography using robust prediction of specimen movements. J. Struct. Biol. 152, 36–51.

Meyer, J.C., Geim, A.K., Katsnelson, M.I., Novoselov, K.S., Booth, T.J., Roth, S., 2007. The structure of suspended graphene sheets. Nature 446, 60–63.

Mitchell, D.R.G., 2008. DiffTools: electron diffraction software tools for Digital Micrograph™. Microsc. Res. Tech. 71, 588–593.

Miyazawa, A., Fujiyoshi, Y., Stowell, M., Unwin, N., 1999. Nicotinic acetylcholine receptor at 4.6Å resolution: transverse tunnels in the channel. J. Mol. Biol. 288, 765–786.

Nair, R.R., Blake, P., Blake, J.R., Zan, R., Anissimova, S., Bangert, U., Golovanov, A.P., Morozov, S.V., Geim, A.K., Novoselov, K.S., Latychevskaia, T., 2010. Graphene as a transparent conductive support for studying biological molecules by transmission electron microscopy. Appl. Phys. Lett. 97, 153102–153103.

Pantelic, R.S., Meyer, J.C., Kaiser, U., Baumeister, W., Plitzko, J.r.M., 2010. Graphene oxide: a substrate for optimizing preparations of frozen-hydrated samples. J. Struct. Biol. 170, 152–156.

Pantelic, R.S., Suk, J.W., Hao, Y., Ruoff, R.S., Stahlberg, H., 2011a. Oxidative doping renders graphene hydrophilic, facilitating its use as a support in biological TEM. Nano Lett. 11, 4319–4323.

Pantelic, R.S., Suk, J.W., Magnuson, C.W., Meyer, J.C., Wachsmuth, P., Kaiser, U., Ruoff, R.S., Stahlberg, H., 2011b. Graphene: substrate preparation and introduction. J. Struct. Biol. 174, 234–238.

Rader, R.S., Lamvik, M.K., 1992. High-conductivity amorphous TiSi substrates for low-temperature electron microscopy. J. Microsc. 168, 71–77.

Regan, W., Alem, N., Aleman, B., Geng, B.S., Girit, C., Maserati, L., Wang, F., Crommie, M., Zettl, A., 2010. A direct transfer of layer-area graphene. Appl. Phys. Lett., 96.

Rhinow, D., Kuhlbrandt, W., 2008. Electron cryo-microscopy of biological specimens on conductive titanium-silicon metal glass films. Ultramicroscopy 108, 698–705.

Rhinow, D., Vonck, J., Schranz, M., Beyer, A., Golzhauser, A., Hampp, N., 2010. Ultrathin conductive carbon nanomembranes as support films for structural analysis of biological specimens. Phys. Chem. Chem. Phys. 12, 4345–4350.

Rhinow, D., Weber, N.-E., Turchanin, A., Golzhauser, A., Kuhlbrandt, W., 2011a. Single-walled carbon nanotubes and nanocrystalline graphene reduce beam-induced movements in high-resolution electron cryo-microscopy of ice-embedded biological samples. Appl. Phys. Lett. 99, 133701–133703.

Rhinow, D., Buenfeld, M., Weber, N.-E., Beyer, A., Golzhauser, A., Kuhlbrandt, W., Hampp, N., Turchanin, A., 2011b. Energy-filtered transmission electron microscopy of biological samples on highly transparent carbon nanomembranes. Ultramicroscopy 111, 342–349.

Turchanin, A., Weber, D., Buenfeld, M., Kisielowski, C., Fistul, M.V., Efetov, K.B., Weimann, T., Stosch, R., Mayer, J., Golzhauser, A., 2011. Conversion of self-assembled monolayers into nanocrystalline graphene: structure and electric transport. ACS Nano 5, 3896–3904.

Yoshioka, C., Carragher, B., Potter, C.S., 2010. Cryomesh: a new substrate for cryo-electron microscopy. Microsc. Microanal. 16, 43–53.

Zhou, Z.H., Prasad, B.V.V., Jakana, J., Rixon, F.J., Chiu, W., 1994. Protein subunit structures in the herpes simplex virus a-capsid determined from 400 kV Spot-scan electron cryomicroscopy. J. Mol. Biol. 242, 456–469.